===== **REVIEWS** =====

Supersmooth and Modified Surface of Sapphire Crystals: Formation, Characterization, and Applications in Nanotechnologies

A. E. Muslimov[a],*, V. E. Asadchikov[a], A. V. Butashin[a], V. P. Vlasov[a], A. N. Deryabin[a], B. S. Roshchin[a], S. N. Sulyanov[a,b], and V. M. Kanevsky[a]

[a] *Shubnikov Institute of Crystallography, Federal Scientific Research Centre "Crystallography and Photonics," Russian Academy of Sciences, Leninskii pr. 59, Moscow, 119333 Russia*

[b] *National Research Centre "Kurchatov Institute", pl. Akademika Kurchatova 1, Moscow, 123182 Russia*

*e-mail: amuslimov@mail.ru

Received May 10, 2016

Abstract—The results of studying the state of the surface of sapphire crystals by a complex of methods in different stages of crystal treatment are considered by an example of preparing sapphire substrates with a supersmooth surface. The possibility of purposefully forming regular micro- and nanoreliefs and thin transition layers using thermal and thermochemical impacts are considered. The advantages of sapphire substrates with a modified surface for forming heteroepitaxial CdTe and ZnO semiconductor films and ordered ensembles of gold nanoparticles are described. The results of the experiments on the application of crystalline sapphire as a material for X-ray optical elements are reported. These elements include total external reflection mirrors and substrates for multilayer mirrors, output windows for synchrotron radiation, and monochromators working in the reflection geometry in X-ray spectrometers. In the latter case, the problems of the defect structure of bulk crystals sapphire and the choice of a method for growing sapphire crystals of the highest structural quality are considered.

CONTENTS

INTRODUCTION

Currently, single-crystal sapphire (α-Al$_2$O$_3$) is widely used in industry as a material for substrates, windows, laser and dispersion elements, crucibles, etc. Sapphire substrates are used, in particular, to grow epitaxial Si (silicon-on-saphire (SOS) structures), GaN, InN, AlN, and GaP layers for integrated circuits; blue, green, and white light-emitting diodes (LEDs); laser diodes; and RF transistors [1]. Sapphire windows are also used in furnaces, vacuum systems, fire-alarm systems, deep-water chambers, and aviation technology [2, 3] (i.e., in the fields where devices must operate under extreme conditions), as well as in watches. Sapphire tubes and crucibles are applied in commercial and laboratory equipment to carry out physical and chemical processes in corrosive media and vacuum, at high temperatures, etc. The role of single-crystal sapphire as a laser material is also very important: the first laser was developed using an artificial ruby crystal, i.e., a sapphire crystal containing impurity Cr^{3+} ions as an active element [4]. Sapphire crystals activated with titanium ions became active media of lasers characterized by a uniquely wide wavelength tuning range, ultrashort pulses, and extremely high radiation power [5, 6]. Currently, sapphire crystals are considered promising materials of monochromators for experiments with synchrotron radiation beams and X-ray lasers [7, 8].

The wide application of sapphire is due to its high technological efficiency and unique combination of properties; some of them [9—11] are listed in Table 1. Sapphire crystals are not dissolved in water and do not absorb moisture from air; they are also stable to mineral acids (at temperatures up to 300°C) and alkali and metal melts (up to 800°C). Along with chemical durability, sapphire crystal is characterized by high radiation resistance. Among dielectric crystals, sapphire has the highest hardness and very large values of thermal conductivy, resistivity, and bulk laser damage

Table 1. Some properties of sapphire (α-Al$_2$O$_3$) crystals

T_{melt}, °C	~2040
Thermal conductivity, W·cm^{-1} K^{-1}	0.35 ∥ c axis
	0.33 ⊥ c axis
Thermal-expansion coefficient, 10^{-6} K^{-1}	5.31 ∥ c axis
	4.78 ⊥ c axis
Density, g cm^{-3}	3. 99
Mohs hardness	9
Knoop hardness, kg mm^{-2}	2100
Optical transparency range, µm	0.14–6.5
Refractive indices (at $\lambda = 0.694$ µm)	$n_o = 1.763$
	$n_e = 1.755$
Laser breakdown threshold (bulk), J cm^{-2}	210
Resistivity (at 293 K), 10^{18} Ω cm	≥5
Permittivity of free space ε_o	10.6 ∥ c axis
	8.6 ⊥ c axis
Solubility in water	no

threshold. The range of optical transparency of sapphire crystals is rather wide: from UV to the mid-IR range. Sapphire α-Al$_2$O$_3$ melts congruently, has a low saturated vapor pressure, and does not undergo any polymorphic phase transitions upon cooling from the melting temperature. Therefore, the most efficient growth techniques can be used to obtain sapphire single crystals such as the Verneuil, Czochralski, Stepanov, Kyropoulos–Musatov, Schmid–Viechnicki, and Bagdasarov methods [12, 13].

Since sapphire crystals are characterized by high hardness and chemical durability, the fabrication of crystalline sapphire elements and details is a separate and very important part of the technology of this material, which includes the mechanical treatment of the crystal surface by abrasive materials, the oriented cutting of a crystal into preforms, and the subsequent grinding and polishing of their surfaces [14]. In this review we report the latest data on the state of the surface of sapphire crystals in different stages of their

treatment by the example of preparing sapphire substrates with a supersmooth surface. Possibilities of various modifications of the sapphire surface using thermal and thermochemical impacts are considered, and advantages of sapphire substrates with a modified surface for forming heteroepitaxial $A^{II}B^{VI}$ semiconductor films and ordered ensembles of Au nanoparticles are presented. The results of the latest experiments on the application of sapphire crystals as a material for X-ray optical elements are reported.

1. SURFACE ROUGHNESS AND ATOMICALLY SMOOTH STEPS

When fabricating functional elements from sapphire crystals, either a free or bound abrasive is used; however, in any case, the average grain size of the abrasive is always successively reduced in order to minimize the roughness of the processed surface and the depth of the damaged surface layer [14–16]. Let us consider these operations in more detail by the example of fabrication of sapphire substrates for nitride epitaxy. Substrates with a diameter of 50.8 mm, a thickness of ~0.45 mm, and an orientation of (0001) were prepared from sapphire single crystals grown by the Kyropoulos–Musatov method. Substrate preforms were cut by diamond saws and bits and then subjected to grinding and mechanical polishing using abrasive powders or tools based on diamond and boron carbide; the chemical mechanical polishing of the substrates was performed on a polyurethane lap using a silica-sol-based suspension (Table 2).

The final stages of all operations are washing preforms and measuring controlled parameters. In particular, the relief and surface roughness R_a for operations 1–4 (Table 2) were measured by a mechanical profilometer, whereas atomic force microscopy (AFM) and X-ray scattering were used for operations 5–8 [17]. The damaged-layer depth after the operations was defined as the thickness of the surface layer that must be removed by chemical mechanical polishing or etched until the formation of terrace-step nanostructures (TSNs) on the surface and a change in the width

Table 2. Sequence of technological operations in the fabrication of sapphire substrates with a supersmooth surface

No.	Operation	Abrasive-grain size, µm	Damaged-layer depth, µm	Surface roughness R_a, µm
1	Cutting	28–100	50–150	0.4–1.5
2	Grinding (1st stage)	28–63	50–100	0.4–1.0
3	Grinding (2nd stage)	14–28	20–50	0.2–0.4
4	Mechanical polishing (1st stage)	3–10	5–20	0.05–0.1
5	Mechanical polishing (2nd stage)	0.5–3	1–5	0.005–0.05
6	Chemical mechanical polishing (1st stage)	0.05–0.1	0.05–0.1	0.0003–0.001
7	Chemical mechanical polishing (2nd stage)	0.001–0.01	0.001–0.005	0.0001–0.0003
8	High-temperature annealing		0.0005–0.001	0.0001–0.0002

of X-ray diffraction reflection curves [18, 19]. The results of measuring the roughness and damaged-layer depth for the (0001) surface of sapphire substrate preforms in different treatment stages are listed in Table 2.

It is noteworthy that these values sharply and non-monotonically decrease when switching from mechanical to chemical mechanical treatment of the surface and that the surface morphology radically changes from stochastic to ordered (Fig. 1) with a decrease in roughness to values on the order of crystal unit-cell parameter (the so-called size effect) [18]. This effect can be explained as follows: operations 1–5 (cutting, grinding, and mechanical polishing) lead to the removal of material due to the brittle fracture and plastic deformation of crystal affected by superhard abrasive, which leaves corresponding traces on the crystal surface and enriches the surface layer with microcracks, slip planes, dislocations, misoriented crystallites, etc., thus forming a damaged layer. Being subjected to chemical mechanical polishing (operations 6, 7), sapphire is involved in a chemical reaction with SiO_2, which is present in the polishing suspension, to form compound Al_2SiO_5; the latter is then removed from the sapphire surface by SiO_2 particles [15, 20]. Etching the sapphire surface is mainly nonselective, and the mechanical effect is weak because of the much lower hardness of silica sol particles in comparison with sapphire.

The discreteness of the structure of a supersmooth crystal surface, i.e., the formation of TSNs on it (Fig. 1b), limits a further decrease in roughness. Calculations show that the minimal roughness of vicinal (0001) sapphire plates (the surface plane of which deviates from the crystallographic plane by a small angle $\alpha = 0.1°–5°$) is $R_a = 0.055$ nm [18]. Smaller roughness values can be expected for the substrates whose surface is formed by one atomically smooth face (free of steps); however, there are no data on the fabrication of these substrates or sapphire elements.

The high-temperature annealing of preforms is widely used in the fabrication of sapphire substrates [14]; however, removing residual macroscopic stress after any operation in the 1–6 series, this treatment does not cause any significant changes in the surface relief and roughness and damaged layer depth in preforms. At the same time, the annealing of substrates with a supersmooth surface after chemical mechanical polishing radically changes the structure of their surface [21–28]. In particular, after annealing at a temperature of 900–1000°C, one can observe substrate surface cleaning (from silica sol particles) and significant surface smoothing without changing the TSN step height (Fig. 2). An increase in the annealing temperature above 1000°C leads to a coarsening of steps and increase in their height (Fig. 3), as a result of which the substrate surface roughness increases [18].

When choosing the temperature and conditions of substrate annealing, one must take into account the
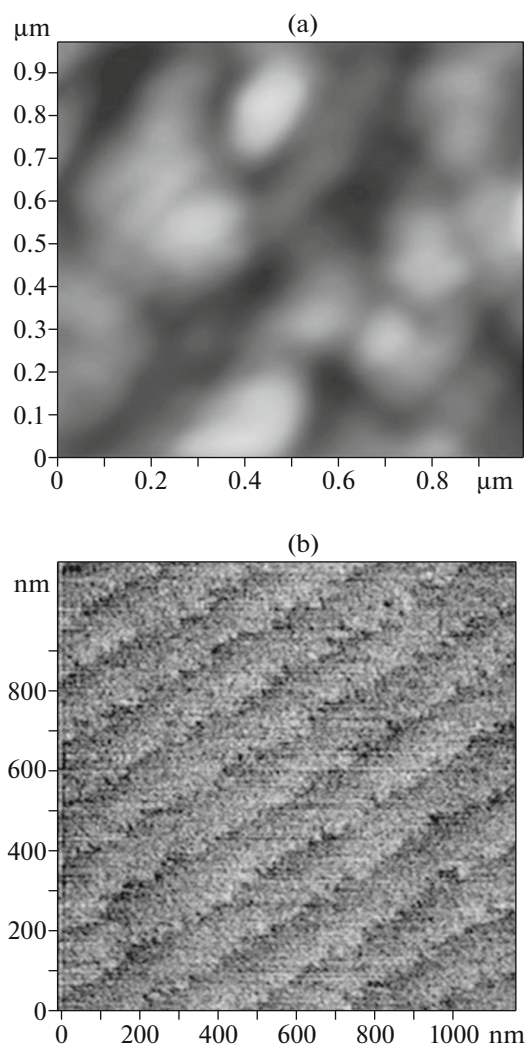

Fig. 1. AFM images of the (0001) sapphire substrate surface after (a) mechanical and (b) chemical mechanical polishing. The measured roughness values for the scans in panels a and b are, respectively, $R_a \sim 1.0$ and 0.1 nm.

difference in the physicochemical processes occurring in the sapphire surface layer. In particular, low-energy electron diffraction and Auger spectroscopy studies revealed that vacuum annealing at temperatures >1200°C leads to the deviation of sapphire Al_2O_3 from stoichiometry because of the loss of oxygen and formation of structures differing from sapphire on the substrate surface [28, 29].

Concerning annealing in air at temperatures below 1400°C, high-energy electron diffraction (HEED) experiments do not reveal any structural changes on the surface of sapphire substrates; high-resolution transmission electron microscopy (HRTEM) also indicates the conservation of a sapphire structural motif (Fig. 4).

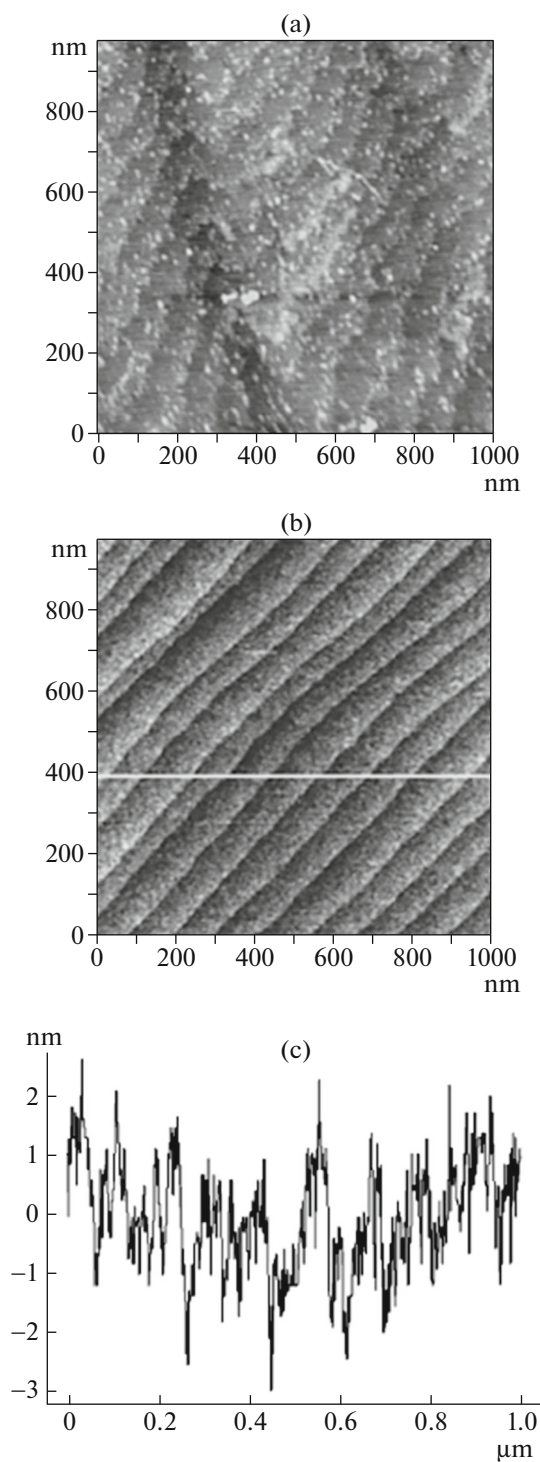As a result of the experiments on annealing sapphire plates in air and vacuum [28], TSNs with desired

Fig. 2. AFM images of the sapphire substrate surface ($\alpha = 0.1°$) after (a) chemical mechanical polishing and (b) subsequent vacuum annealing at 900°C; (c) surface cross section profile after annealing.
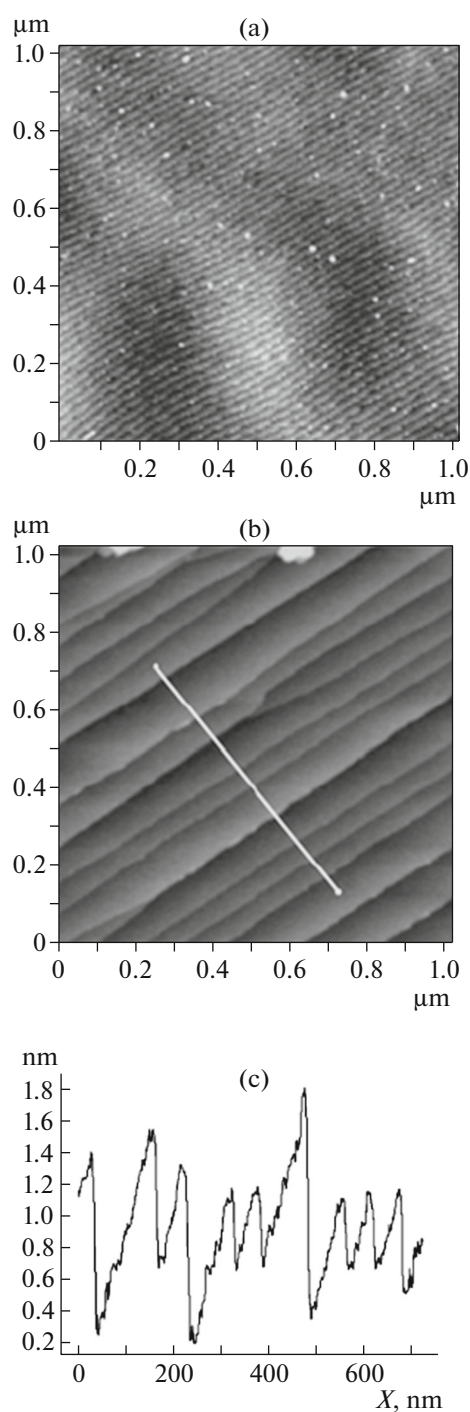

Fig. 3. AFM image of the sapphire plate surface with $\alpha = 0.5°$ after chemical mechanical polishing (a) without annealing and (b) after annealing in air at 1200°C; (c) Surface cross section profile for an annealed sapphire plate.

parameters were fabricated (Table 3). These structures generally satisfy the relation

$$h = d\tan\alpha, \qquad (1)$$

where h is the TSN step height (multiple of 0.22 nm), d is the TSN step width, and α is the vicinal angle.

Along with the aforementioned methods for monitoring the morphology, composition, and structure of the surface of crystalline sapphire elements, optical
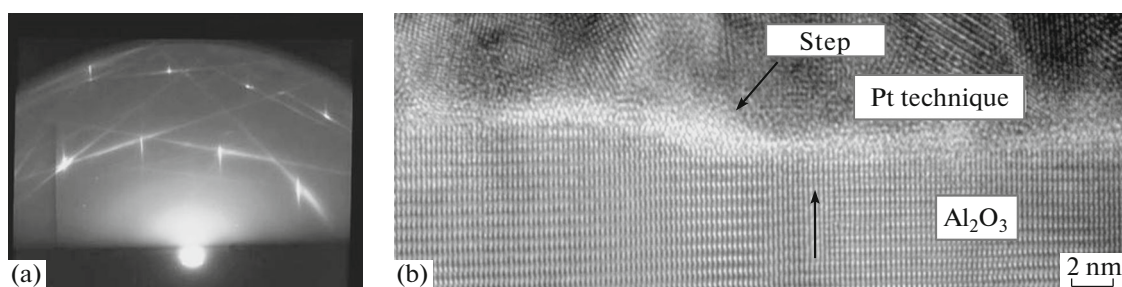
Fig. 4. (a) HEED pattern and (b) bright-field HRTEM image of a single step on the sapphire substrate surface after annealing.

methods [30], X-ray photoelectron spectroscopy [27], X-ray reflectivity [31], and other techniques are also used. As for the theoretical concepts about steps on vicinal crystal surfaces, there is a rather complete review [32], which is, however, focused on crystals with covalent and metallic bonds. The dependence of the TSN parameters on the vicinal angle of sapphire plates and annealing temperature was considered in [24, 28, 33].

2. HETEROEPITAXY OF $A^{II}B^{VI}$ COMPOUNDS ON SAPPHIRE

Cadmium telluride (CdTe) crystals, which belong to the group of semiconductor compounds $A^{II}B^{VI}$, are used as substrates to grow epitaxial CdHgTe layers for IR detectors and fabricate sensing elements for X-ray and γ detectors. They attract the attention of researchers as a promising material for modern photonics. Crystals of another representative of the $A^{II}B^{VI}$ family—zinc oxide (ZnO)—are used to fabricate detectors and sensors of different types; they are also considered substrates for growing GaN-based heterostructures in optoelectronics.

However, the growth of these crystals from melt is hindered by intense evaporation of the melt components and the existence of a series of high-temperature polymorphic phase transitions in CdTe. An alternative to bulk ZnO and CdTe crystals is epitaxial films grown on different crystalline substrates. Films are obtained using molecular-beam epitaxy, metal-organic chemical vapor deposition, laser ablation, and magnetron sputtering [34—39]. Among applicable single-crystal substrates, (0001) sapphire (α-Al_2O_3) plates are most popular. The lattice parameters of ZnO, CdTe, and Al_2O_3 are listed in Table 4. Note that heteroepitaxial ZnO and CdTe films contain twins and domains with differently oriented polar axes; moreover, these films have a rough surface [34—39].

The influence of pre-epitaxial thermal treatment of Al_2O_3 (0001) substrates on the structure of ZnO and CdTe films grown by magnetron sputtering and molecular-beam epitaxy, respectively, was studied in [43, 44]. Epitaxial growth of ZnO and CdTe films occurred on only sapphire substrates subjected to annealing in air and containing a system of smooth terraces and steps (Fig. 5). Indexing of the corresponding electron diffraction patterns showed that the

Table 3. TSN step heights (nm) for different vicinal angles α and annealing temperatures of sapphire plates in air and in vacuum ($P_{res} \sim 0.13$ Pa)

Plate misorientation angle α, deg	Annealing temperature, °C						
	1000		1100	1200		1300	1400
	air	vacuum	vacuum	air	vacuum	air	air
0.03	0.22						
0.1	0.22	0.22	0.22	0.22	0.22	0.22–0.6	
0.2	0.22	0.22			0.4–0.8		
0.3	0.22	0.22		1–3	0.8–1	1–2	1–2
0.5	0.22	0.22	1.5–2	0.4–2.2	0.8	0.6–1.8	
1.0	×	×	0.2–0.4*	0.4–1.2	1	1–3	
3.0	×			1–2			2–7
5.0	×			1–5			1.5–5.5

* TSNs are highly irregular.

Table 4. Structural data on ZnO, CdTe, AlN, and Al_2O_3 crystals

Composition	Structure type	Sp. gr.	a, nm	c, nm	Z	References
Al_2O_3	Corundum	$R\bar{3}c$	0.47540(5)	1.29820(6)	6	[40]
ZnO	Wurtzite	$P6_3mc$	0.3249(6)	0.52042(20)	2	[41]
CdTe sphalerite	$F\bar{4}3m$	$F\bar{4}3m$	0.64827(8)	–	4	[42]
AlN	Wurtzite	$P6_3mc$	0.3112	0.4982	2	[46]

(0001) plane of ZnO films is oriented parallel to the substrate when the following relationship is valid:

$$(0001)[10\bar{1}0]ZnO\|(0001)[11\bar{2}0]Al_2O_3. \qquad (2)$$

During the growth of CdTe films, the octahedron face is oriented parallel to the basal sapphire face:

$$(111)[1\bar{1}0]CdTe\|(0001)[11\bar{2}0]Al_2O_3. \qquad (3)$$

Growth of block textured ZnO films or unoriented polycrystalline CdTe films was observed on the surface of the substrates subjected to only chemical mechanical polishing and the substrates annealed in vacuum ($P < 0.13$ Pa) and containing TSNs. The absence of CdTe epitaxial growth and the existence of ZnO mosaicity are apparently caused by the presence of structural defects (vacancy clusters and displaced atoms) on the substrate surface after polishing, which impede oriented nucleation and film growth. In turn, annealing in vacuum leads to the deviation of aluminum oxide from stoichiometry and causes lattice distortion [28, 29]; these factors also hinder nucleation.

An analysis of the electron diffraction patterns of epitaxial CdTe films shows that they are mosaic and contain twins with the $\langle 111 \rangle$ twinning axis. It is likely that these films also contain crystallites obeying the relationship

$$(111)[11\bar{2}]CdTe\|(0001)[11\bar{2}0]Al_2O_3, \qquad (4)$$

and specifically these crystallites are responsible for the occurrence of weak additional reflections in the electron diffraction pattern of CdTe film (Fig. 5b). The AFM surface image of epitaxial CdTe film exhibits crystallites with lateral sizes of about 50 nm. Proceeding from the crystallite habit, one can conclude that the film contains twins oriented in correspondence with relationships (3) and (4).

Additional studies of the growth of CdTe films on the structured (0001) sapphire surface, oriented at an angle of 44° with respect to the vapor flow direction and normally to the direction of steps (oriented in the $[11\bar{2}0]$ direction), were performed. This geometry of the substrate (heated to a temperature of 300°C) and vapor source was found to provide growth of single-crystal CdTe films if the step height exceeds 1 nm. These results are explained by the occurrence of a longitudinal component of the diffusion flow of CdTe molecules and atoms towards the steps from the internal side and their repulsion from the edge step from the external side due to the presence of Schwoebel–Ehrlich barrier; the latter provides the efficient supply of material and necessary supersaturation for the nucleation on the step edge and growth of oriented CdTe islands. The thus obtained cadmium telluride films have an orientation corresponding to (3), and their composition is close to the CdTe stoichiometry [45].

The structural quality of epitaxial ZnO films is better than that of CdTe films, and the surface morphology indicates that the crystallites (Fig. 5a) are oriented with respect to the substrate according to relation-
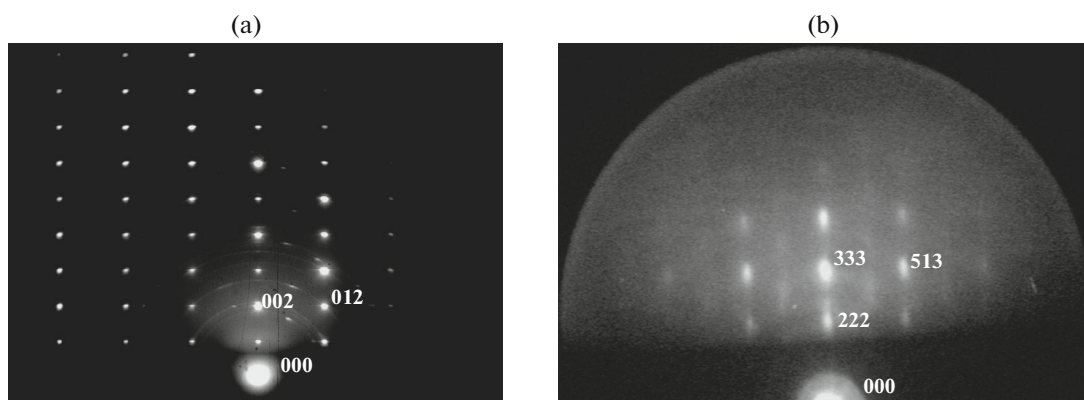

Fig. 5. Electron diffraction patterns of (a) ZnO and (b) CdTe films grown on sapphire substrates and annealed in air at 1000°C.

ship (2). The presence of additional reflections in the electron diffraction patterns of ZnO films grown on sapphire substrates subjected to chemical mechanical polishing or annealed in vacuum indicates the existence of crystallites obeying the relationship

$$(0001)[11\overline{2}0]ZnO\|(0001)[11\overline{2}0]Al_2O_3. \qquad (5)$$
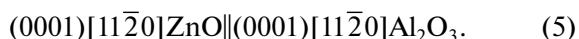
A possible reason for such large differences in the structural quality of epitaxial ZnO and CdTe films grown on (0001) sapphire substrates, with allowance for the fact that the growth rate of ZnO films multiply exceeds that of CdTe films in this case, is that the lattice mismatch of CdTe and sapphire is only 3.7% for both orientational relationships, (3) and (4) [38]. This mismatch for the ZnO/sapphire pair is 18.4% for relationship (2) and 31.8% for relationship (5) [39]. Thus, the mosaicity of the ZnO film/sapphire structure is suppressed due to the decrease in the elastic energy contribution to the total energy of the film/substrate system in the former case.

The significant mismatch between the substrate and epitaxial film can be overcome in another way: by forming buffer layers. For ZnO films on (0001) sapphire substrates, the most appropriate version is an aluminum nitride layer, which is isostructural to ZnO and has similar lattice parameters [46]. This layer can also be obtained by thermochemical nitridation of sapphire substrate: heating the latter in a mixture of N_2, CO, and H_2 gases [47]. The corresponding studies were performed using scanning electron microscopy (**SEM**), scanning transmission electron microscopy (**STEM**), and energy-dispersive X-ray microanalysis (**EDXMA**). The transvers-cut STEM data (Fig. 6) revealed the formation of a continuous aluminum nitride (AlN) film with a thickness of about 100 nm and a sharp AlN/Al_2O_3 interface on the sapphire substrate surface after thermochemical nitridation. The EDXMA data confirm the complete nitridation of the sapphire substrate surface to a depth of about 100 nm.

According to the reflection high-energy electron diffraction data, the surface of sapphire substrates subjected to thermochemical nitridation contains a single-crystal AlN phase with a hexagonal wurtzite structure (Fig. 7, inset). Indexing of the electron diffraction pattern shows that the AlN film is oriented by the (0001) plane parallel to the substrate surface and consists of slightly misoriented blocks. The nitride film surface exhibits defects (Fig. 7) in the form of characteristic hexagonal etching pits with linear sizes up to 200 nm and a height up to 10 nm. The presence of these defects significantly increases the substrate surface roughness (up to 4−5 nm).

The surfaces of ZnO films on nitridized substrates have a grain microstructure with grain sizes on the order of 50−70 nm (Fig. 8). The surface contains craters with linear sizes up to 1 μm and a depth of up to 50 nm, which are presumably formed on substrate surface defects. An analysis of the electron diffraction
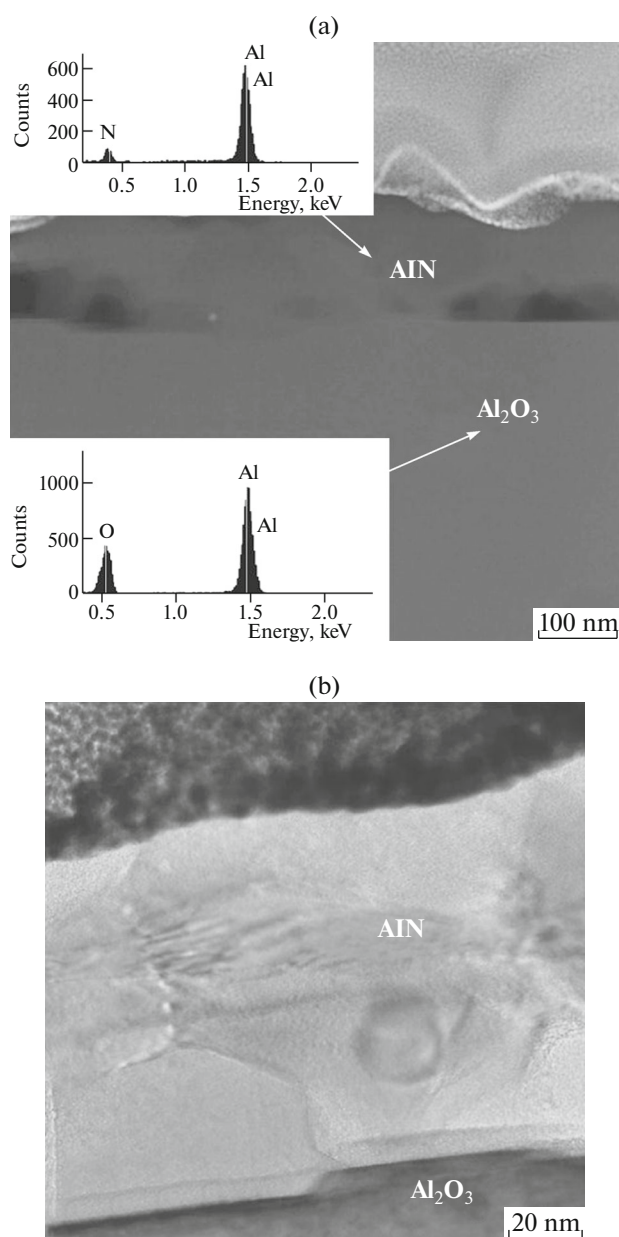

Fig. 6. STEM image of a transverse cut of the sapphire substrate surface after thermochemical nitridation in an electron microscope obtained using a high-angle dark-field ring detector and the EDXMA data on the heterostructure for different depths (insets).

pattern shows (Fig. 8, inset) that ZnO films are crystallized into a wurtzite-type structure and grow with the (0001) plane oriented parallel to the AlN and Al_2O_3 (0001) planes. Film are slightly mosaic; however, the aforementioned domains and twins are suppressed in them. Electron diffraction patterns of epitaxial ZnO films grown on sapphire substrates subjected to chemical mechanical polishing but without thermochemical nitridation exhibited additional reflections and even rings. This feature may indicate not only the formation
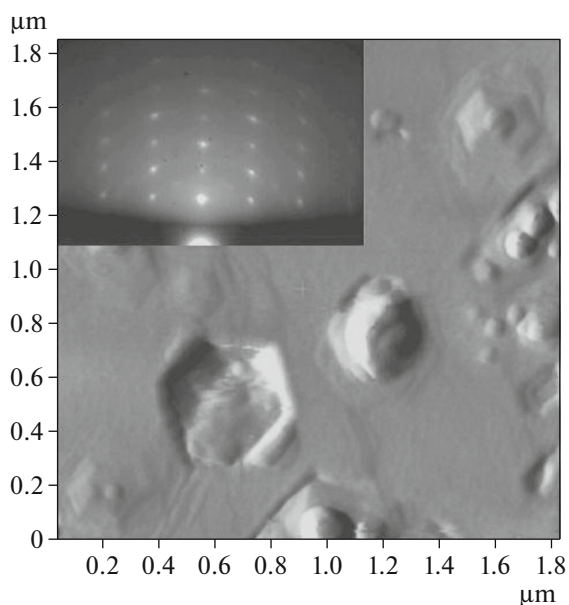
Fig. 7. AFM image (contact scanning mode) of the (0001) sapphire substrate surface after thermochemical nitridation and its electron diffraction pattern (inset).
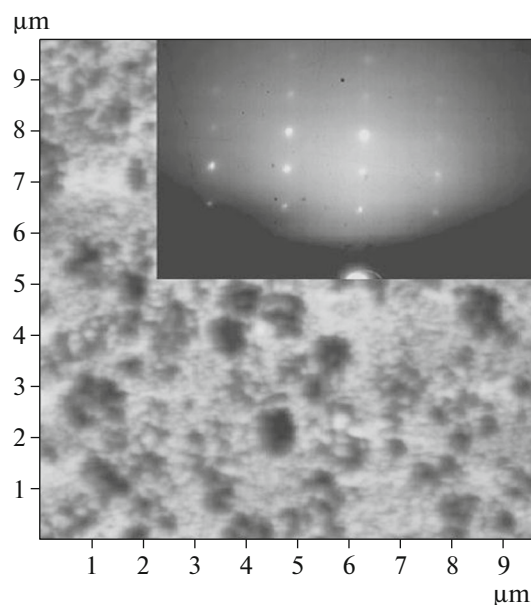

Fig. 8. AFM image of a zinc oxide film on a (0001) sapphire substrate with nitridized surface and the corresponding electron diffraction pattern (inset).

of domains and twins in a ZnO film, but also the presence of randomly oriented crystallites in it.

Figure 9 shows the experimental rocking curves from the (002) planes of epitaxial ZnO films in two structures: ZnO/Al_2O_3 and $ZnO/AlN/Al_2O_3$. A comparison of the rocking curves of these crystal structures shows that, in the case of the $ZnO/AlN/Al_2O_3$ structure, the intensity of the ZnO (002) reflection is much higher (by a factor of about 800) and the half-width of the FWHM curve is much smaller (by a factor of about 7) than for the ZnO/Al_2O_3 structure. Like the HEED data, the X-ray diffraction data give grounds to state that thermochemical nitridation of the (0001) sapphire substrate surface improves significantly the structural quality of epitaxial ZnO films. Obviously, a facilitating factor is that the ZnO and AlN compounds belong to the same structure type (wurtzite) and have similar unit-cell parameters.

In addition, with allowance for the rotation of the wurtzite and sapphire lattices by 30° during epitaxy in the case under consideration (2) $((0001)[10\bar{1}0]ZnO\|(0001)[11\bar{2}0]Al_2O_3)$, the unit-cell parameters of both crystalline layers and substrate satisfy the relationship $a_{ZnO}\sqrt{3} > a_{AlN}\sqrt{3} > a_{Al2O3}$ (Table 4). The presence of an intermediate AlN layer with a unit-cell parameter a improves the lattice matching between the epitaxial ZnO film and sapphire substrate, reducing the stress at the interface. Note that the difference in parameters a of the AlN films and substrate is rather large (13.4%); due to this, differently oriented domains arise in AlN films during thermochemical nitridation (Fig. 6b). However, the

concentration of domains and twins in AlN films is relatively low, which is apparently related to the mechanism of AlN film formation: a solid-phase chemical reaction during nitrogen diffusion with the replacement of oxygen on the sapphire substrate surface.

3. GOLD FILMS ON SAPPHIRE

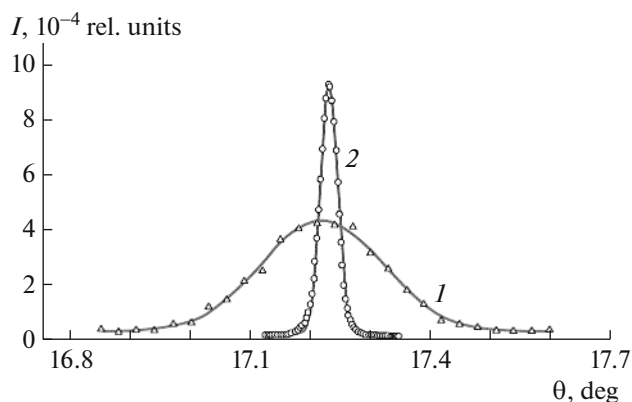Ordered ensembles of metal nanoparticles are interesting and promising objects both for designing

Fig. 9. Experimental rocking curves from the (002) planes in a ZnO film: (*1*) the sample without an AlN buffer layer and (*2*) the sample with an AlN buffer layer. Symbols are experimental data and solid lines are approximations by a Gaussian at the peak half-width: (*1*) 0.237° and (*2*) 0.034°. The intensity normalized to the incident beam intensity is indicated. The intensity of curve *1* is multiplied by 350.
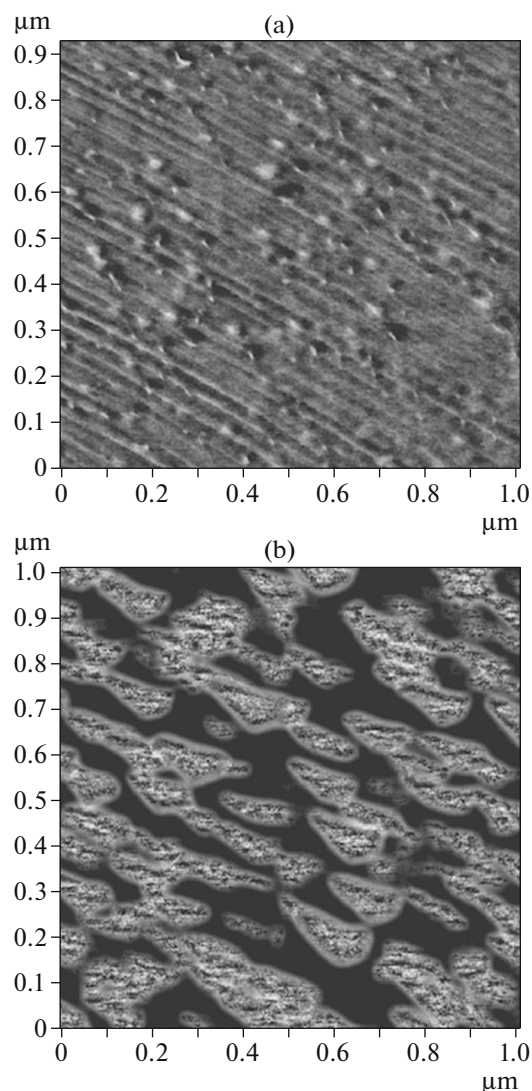
Fig. 10. AFM images of a substrate with a deposited gold film after 1-h annealing at T = (a) 400 and (b) 600°C.

Fig. 11. AFM images of structured gold nanoparticles on a sapphire surface (1-h annealing at T = 900°C).

[54], after which this composite structure was annealed in air. Annealing at 400°C for 1 h causes the formation of rare islands about 20−30 nm in size (Fig. 10a). A 1-h annealing to 600°C leads to further coarsening of islands (Fig. 10b), which form ordered ensembles on the surface due to the orienting effect of ordered nanostructures from regular terraces and steps on the sapphire substrate surface. Then the islands coalesce to form inhomogeneous filaments 200−400 nm long.

Annealing at 900°C leads to the complete structurization of a gold film with formation of particles about 4−6 nm high with a diameter of 80−100 nm, which corresponds to the step period at the object localization site (Fig. 11).

Thus, Au atoms were found to have enhanced diffusion mobility, which is caused by the nanoscale effect at temperatures much lower than the melting temperature of gold particles (1063°C). The nanostructured sapphire substrate surface organizes the formation of ordered ensembles of Au particles on it.

Samples annealed at 900°C with nanocrystals ∼80−100 nm in size (formed on a flat substrate along the steps of terrace structure on a sapphire surface) were chosen for optical studies. An analysis of the angular dependence of scattered radiation shows that the relief is ordered and the absence of diffraction peaks indicates that its characteristic period is smaller than the probe radiation wavelength.

Having experimental data on the angular dependence of reflectance, one can obtain an experimental curve and compare it with the theoretical one. The dependence of the reflectance amplitude on the angle of incidence is given by the Fresnel formulas

chemical and biological sensors and for photonics applications [48−52]. One of the main methods for forming these ensembles is visible-light photolithography [53] (with a wavelength of about 1 μm); however, the particle size is restricted by the diffraction limit from below. The possibilities of artificial (grapho-) epitaxy are also limited, because this technique cannot yet provide submicron elements. In contrast, the potential of ion or electron etching is limited from above: the maximum sizes of processed areas are several tens or, at best, several hundreds of micrometers. Therefore, an urgent problem is to develop a technique for forming ordered ensembles of metal nanoparticles using the structuring influence of nanoscale substrate profile. In particular, a gold film with a thickness of about 1−2 nm was previously deposited on a TSN-containing sapphire substrate by magnetron sputtering
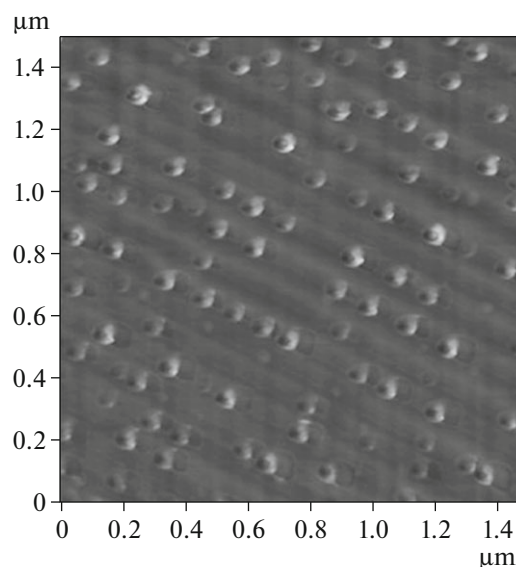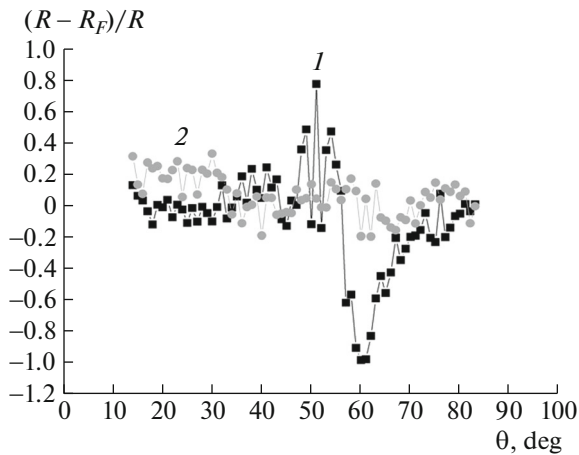
$(R - R_F)/R$

Fig. 12. Angular dependences of the $R_P - R_{FP})/R_P$ ratio for (*1*) *p*- and (*2*) *s*-polarized incident waves.

$$R_{FS} = \frac{\cos\theta - \sqrt{n^2 - \sin^2\theta}}{\cos\theta + \sqrt{n^2 - \sin^2\theta}} - \text{for } s \text{ polarization,}$$

$$R_{FP} = \frac{n^2\cos\theta - \sqrt{n^2 - \sin^2\theta}}{n^2\cos\theta + \sqrt{n^2 - \sin^2\theta}} - \text{for } p \text{ polarization,}$$

where θ is the angle of incidence and n is the refractive index of the sample (substrate) material. The intensity reflectance is the squared modulus of the aforementioned expressions. Having subtracted the theoretical curve from the experimental dependence, one can investigate the influence of the fine effects related to the nanostructures deposited on the sample. Figure 12 shows the difference between the experimentally found modulus of amplitude reflectance R for *s*- and *p*-polarized light beams (wavelength $\lambda = 488$ nm) and reflectance R_{Fr} calculated from the Fresnel formula and normalized to the experimental value. The refractive index of sapphire at a wavelength of $\lambda = 488$ nm was assumed to be 1.77.

Another way to increase the sensitivity of measurements on nanostructures is to analyze the difference between the experimental reflectances of nanostructures differently oriented with respect to the plane of incidence of *s*- and *p*-polarized beams: $\Delta R = R^0 - R^{90}$. Here, R^0 and R^{90} are the sample reflectances for the cases where structures are located, respectively, parallel and perpendicular to the plane of incidence. The presence of fine features in dependence $\Delta R_s(\theta)$ allows one to draw conclusions about the surface structure; however, to compare experimental results with the parameters of surface nanostructures, one needs a theoretical model. For a while one can suggest that, at a certain angle of incidence, the local intensity of electromagnetic field in metal nanospheres located along the terraces on the sapphire surface significantly increases and thus changes the reflection conditions for electromagnetic waves.

The oriented growth of gold films from vapor phase on a (0001) sapphire substrate was implemented in [55]. This growth occurs upon substrate heating to 500°C. Epitaxy is observed when gold nanocrystals reach a certain size at fixed external parameters. Under conditions of weak adhesion between the crystal and substrate, gold is crystallized on edges of atomically smooth substrate steps in the form of nanocrystals, with the conservation of mainly three epitaxial relationships: with high-density atomic planes (111), (100), and (211), oriented parallel to the (0001) Al_2O_3 plane. At lower temperatures gold is crystallized on the substrate in the form of nanocrystals 100−120 nm in size ordered along step edges and having no preferred orientation.

4. MICRO- AND NANOSTRUCTURED SAPPHIRE SURFACE: OXIDATION OF Al FILMS

The use of crystalline substrates with a regular micro- or nanorelief during heteroepitaxy is one way to significantly reduce the dislocation density in films grown on sapphire, for example, in GaN−sapphire structures [56]. A regular micro- and nanorelief of desired configuration and size can also be formed using photolithography, with the subsequent etching of the substrate surface in mask windows or growing sapphire layers on its surface [56−58].

A technique allowing one to proceed without photolithography has begun being developed to obtain sapphire plates with a regular microrelief on their surface [59]. In particular, the technique of vacuum deposition of metal through masks with holes 0.2−40 μm in diameter and subsequent annealing was applied in experiments aimed at forming a regular microrelief on the supersmooth surface of sapphire plates (Fig. 13). Optical microscopy, AFM, and RHEED were used to detect it on the surface and monitor its parameters.

The RHEED patterns of a continuous film obtained by this technique indicate that this film is a mosaic sapphire crystal. A similar result was obtained by transmission electron microscopy. A comparison of bright-field HRTEM images of the sapphire substrate and film (Figs. 13, 14) shows that the substrate has a high structural quality, whereas the film has a pronounced mosaic structure with blocks 5−10 nm in size. A larger part of bright-field HRTEM images of the film exhibits characteristic rotational moiré patterns (Fig. 13) with a period of more than 6 nm: these interplanar spacings are absent in sapphire crystals. One possible reason for the poor structural quality of the sapphire film is the presence of cavities in it (Fig. 14), which arise in it during the oxidation of metallic aluminum upon annealing in air and subsequent solid-phase epitaxy. These cavities can be eliminated by reducing the heating rate during annealing or by decreasing the thickness of deposited Al films.
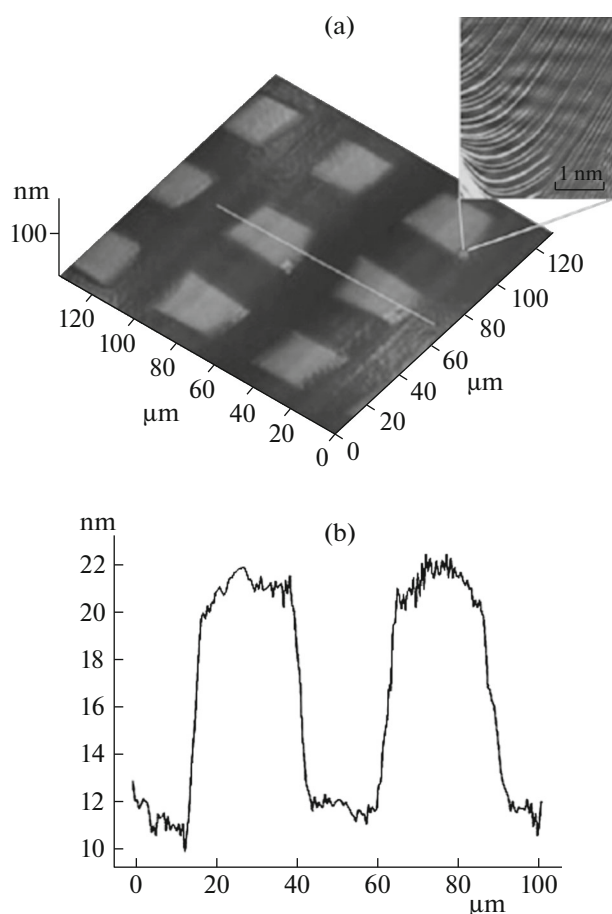
Fig. 13. (a) AFM image and (b) cross-sectional profile of a regular microrelief formed on sapphire plate surface after annealing at 1400°C. The inset shows an AFM image of the lateral surface of mask element.

Fig. 14. Bright-field HRTEM image of the structure of sapphire film near its surface.

substrate surface. The self-organization occurs under different impacts: anodic oxidation, diffusion, and grain growth during annealing.

5. SAPPHIRE AS A MATERIAL FOR X-RAY OPTICAL ELEMENTS

Currently, one of the most widespread materials for X-ray optical elements (both grazing-incidence and diffraction ones) is single-crystal silicon [61]. Recently, in view of the development and spread of ultrabright X-ray sources, such as synchrotrons and X-ray free-electron lasers, researchers are paying attention to sapphire, which is a promising material for X-ray optical elements [62] because of the favorable combination of its acceptable physical characteristics with technological efficiency. The progress in the technology of processing sapphire crystals, which provides, in particular, effective heights of element surface roughness as small as about 0.1 nm [17], opens up ways to fabricate elements of total external reflection mirrors and substrates for multilayer mirrors from sapphire.

In addition, TSNs on a sapphire surface (Figs. 2, 3) can also be used to control X-ray beams: if the structure period is sufficiently constant throughout the entire surface, this structure is a diffraction grating. The crystal is an oxide, because the relief is highly stable in air. Irradiation by a grazing-incidence beam yields a peak in the scattering phase function. The latter is proportional to the power spectral density (PSD) function [63]; hence, when plotting a PSD curve, one will also observe a peak with a spatial frequency corresponding to the effective period of the step structure (Fig. 17). This period is determined by angle α between the X-ray beam propagation direction and the direction of steps in the surface structure. Thus, one can implement a system for controlling X-ray beams in which the beam position can be varied within $1°-2°$ by

A way to form sapphire substrates with a nanostructured surface by anodic oxidation of an aluminum film on a substrate, with subsequent annealing in air, was proposed in [60]. A film of metallic aluminum is formed on a (0001) sapphire substrate by vacuum deposition, after which the composite is subjected to the conventional procedure of anodic oxidation. As a result, an aluminum oxide film with a thickness of several hundreds of nanometers is formed on the substrate surface; the film relief is characterized by the presence of cylindrical through holes about 50 nm in diameter with a density of about 50 holes per μm^2 (Fig. 15). Annealing in air is applied to obtain an oriented sapphire film with a nanostructured surface (Fig. 16), which may be of interest as a substrate for growing heteroepitaxial AlN and GaN films.

We believe that this approach has certain advantages before photolithography when fabricating micro- and nanostructured surfaces, because a nanostructure is formed in this case due to the self-organization of atoms of the aluminum film deposited on the
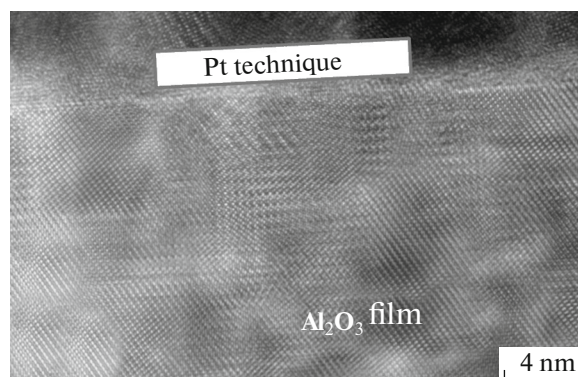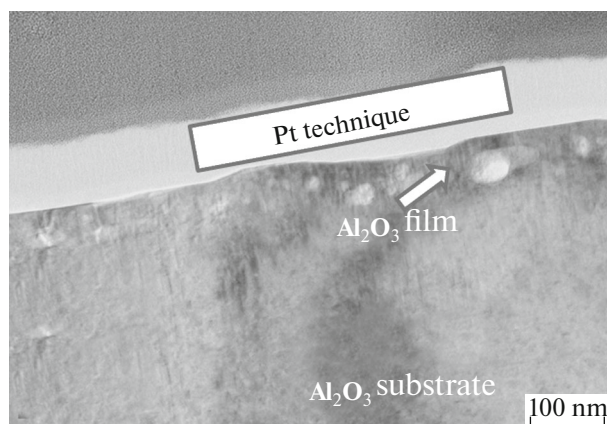
Fig. 15. Bright-field SEM image of the structure of sapphire film near its surface.
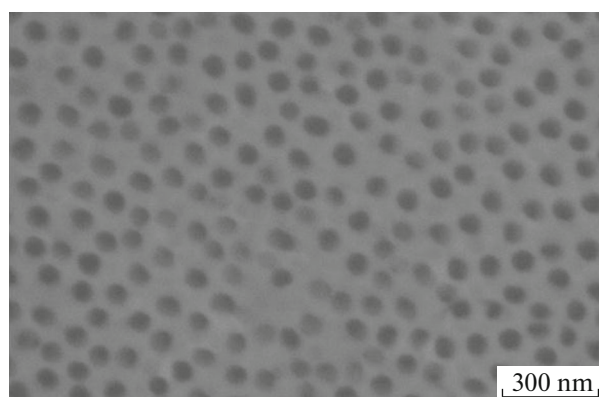

Fig. 16. SEM image of an aluminum oxide film on a (0001) sapphire substrate after anodic oxidation.
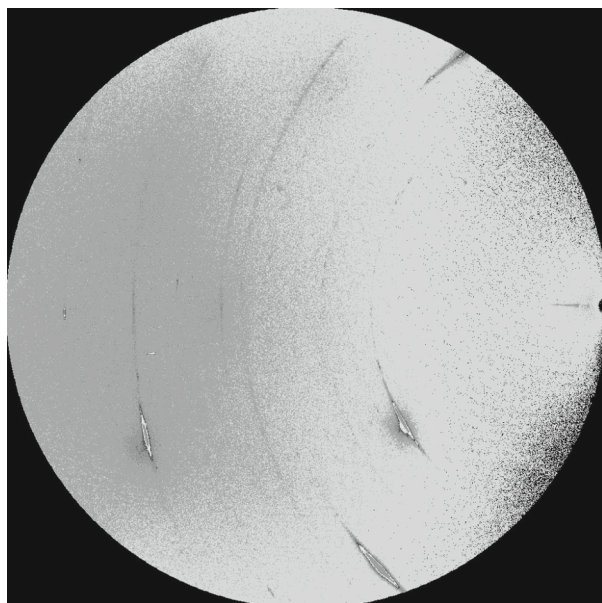

Fig. 17. X-ray diffraction pattern in grazing geometry (synchrotron radiation, $\lambda = 0.9636$ Å) from an aluminum oxide film on a (0001) sapphire substrate after anodic oxidation and subsequent annealing in air at 1400°C.

rotating the reflecting element in the azimuthal plane [62].

Sapphire crystals are also used as output windows for synchrotron radiation, both in the UV [64] and X-ray [65] ranges. In this field of sapphire application, not only the surface characteristic of an element but also its volume characteristics (in particular, transmittance) play an important role. Sapphire is a promising material for monochromators in experiments with synchrotron radiation beams and X-ray lasers [7, 8]; here, the volume characteristics of crystals also play an important role. For example, the first X-ray spectroscopy experiments in the energy range of 20−40 keV, where sapphire monochromators were oriented almost normally to the incident X-ray beam and operated in the reflection geometry, revealed that the necessary values of rocking curve half-width (less than 1 meV) are implemented only in individual portions of the element surface (with an area of about 0.1 mm^2) and the total area of these portions is a small part of the element surface [7]. In a continuation of these studies, a complex X-ray diffraction characterization of the defect structure of sapphire crystals grown by different conventional methods [12, 13] was performed. It was found that the main contribution to the rocking curve broadening is from dislocations [66]. The highest structural quality was observed for the sapphire crystal grown by the Kyropoulos method: the average dislocation density in it was $10^2−10^3$ cm^{-2}, and there were portions about 2×2 mm^2 in size free of dislocation contrast (Fig. 18). Preliminary experiments showed that the structural quality of these sapphire crystals is quite acceptable to use them as monochromators in
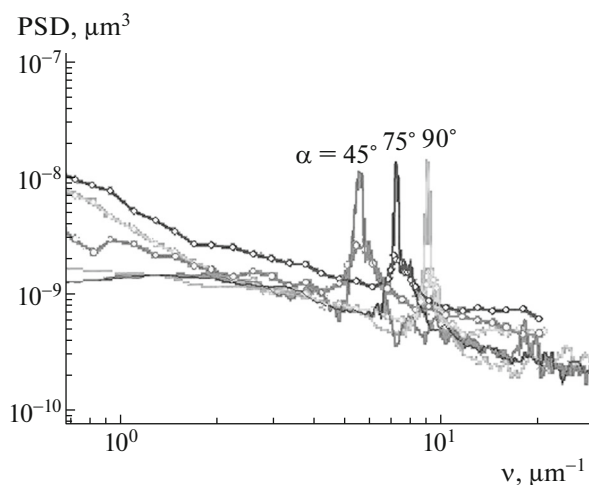

Fig. 18. PSD function of a sapphire surface with a regular relief obtained according to the (circles) X-ray scattering data and (solid lines) AFM data at different angles α of relative primary flat.
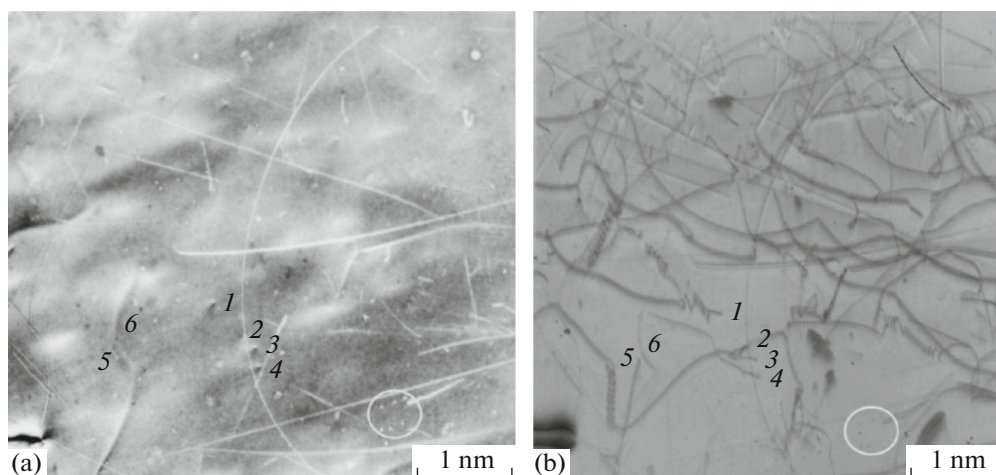
Fig. 19. Comparison of the data of (a) laboratory X-ray topography in the Bragg reflection (b) and white-beam topography for a sapphire sample: the same dislocations are denoted by numbers 1−6. The defects that were also used to identify sample portions are selected by a circle.

X-ray spectrometers operating in the reflection geometry [66].

CONCLUSIONS

In this review we reported the results of studying (using a complex of methods) the surface state of sapphire crystals in different stages of their treatment by the example of preparing sapphire substrates with a supersmooth surface. The possibilities of forming purposefully regular micro- and nanoreliefs and thin transition layers on the sapphire substrate surface by thermal and thermochemical impacts were considered. The advantages of sapphire substrates with a modified surface for forming heteroepitaxial CdTe and ZnO semiconductor films and ordered ensembles of gold nanoparticles were described. The results of the latest experiments on application of crystalline sapphire as a material for X-ray optical elements—total external reflection mirrors, substrates for multilayer mirrors, output windows for synchrotron radiation, and monochromators for X-ray spectrometers operating in the reflection geometry—were presented. In the latter case, problems concerning the defect structure of bulk sapphire crystals and the choice of the method for growing crystals of highest quality were discussed.

REFERENCES

1. Sapphire Applications & Market, *Report,* 2015. www.yole.fr.
2. W. Guiden, Zh. Mingfu, H. Jiecai, et al., Cryst. Res. Technol. **43**, 531 (2008).
3. J. Rioux, C. Jones, M. Mandelartz, and V. Pluen, Adv. Mater. Proc. 31 (2007).
4. T. H. Maiman, Nature **187**, 493 (1960).
5. P. Moulton, Opt. News **8**, 9 (1982).
6. B. K. Sevast'yanov, X. S. Bagdasarov, E. A. Fedorov, et al., Kristallografiya **29** (5), 963 (1984).
7. I. Sergueev, H.-C. Wille, R. P. Hermann, et al., J. Synchrotron Radiat. **18**, 802 (2011).
8. Y. V. Shvyd'ko, *X-Ray Optics: High-Energy-Resolution Applications* (Springer, 2004), **Vol. 98**.
9. F. Gan, *Laser Materials* (World Scientific, Singapore, 1995).
10. M. V. Klassen-Neklyudova, Kh. S. Bagdasarov, L. M. Belyaev, et al*., Ruby and Sapphire* (Nauka, Moscow, 1974) [in Russian].
11. *Handbook of Lasers,* Ed. by A. M. Prokhorov (Sov. Radio, Moscow, 1978), **Vol. 1** [in Russian].
12. Kh. S. Bagdasarov, *High-Temperature Crystallization from Melt* (Fizmatlit, Moscow, 2004) [in Russian].

13. D. C. Harris, Proc. SPIE **7302**, 730202 (2009).

14. *Handbook of Technologist–Optician,* Ed. by Okatov (Politekhnika, St. Petersburg, 2004) [in Russian].

15. Z. C. Li, Z. J. Pei, and P. D. Funkenbusch, Sapphire: Structure, Technology, and Application, Ed. by I. Tartaglia (Nova Science, New York, 2013).

16. E. A. Vovk, Funct. Mater. **22** (2), 252 (2015).

17. V. E. Asadchikov, I. V. Kozhevnikov, B. S. Roshchin, et al., Mir Izmerenii, No. **7**, 11 (2012).

18. A. V. Butashin, A. E. Muslimov, V. M. Kanevskii, et al., Crystallogr. Rep. **58** (3), 483 (2013).

19. I. A. Prokhorov, B. G. Zakharov, B. S. Roshchin, et al., Crystallogr. Rep. **56** (3), 456 (2011).

20. E. A. Vovk, A. T. Budnikov, M. V. Dobrotvorskaya, et al., Poverkhnost, No. **6**, 115 (2012).

21. M. Yoshimoto, T. Maeda, T. Ohnishi, et al., Appl. Phys. Lett. **67**, 2615 (1995).

22. J. Cui, A. Sun, M. Reshichkov, et al., MRS Internet J. Nitride Semicond. Res. **5**, 7 (2000).

23. O. Kurnosikov, L. Pham Van, and J. A. Cousty, Surf. Sci. **459**, 256 (2000).

24. Y. Shiratsuchi, M. Yamamoto, and Y. Kamada, Jpn. J. Appl. Phys. **41**, 5719 (2002).

25. J. R. Heffelfinger and C. B. Carter, Surf. Sci. **389**, 188 (1997).

26. L. Pham Van, O. Kurnosikov, and J. Cousty, Surf. Sci. **411**, 263 (1998).

27. K. G. Saw, J. Mater. Sci. **39**, 1211 (2004).

28. A. V. Butashin, V. P. Vlasov, V. M. Kanevskii, et al., Kristallografiya **57** (5), 927 (2012).

29. T. M. French and G. A. Somorjai, J. Phys. Chem. **74** (12), 2489 (1970).

30. M. Lintz and M.-A. Bouchiat, Surf. Sci. **511**, L319 (2002).

31. Yu. O. Volkov, I. V. Kozhevnikov, B. S. Roshchin, et al., Crystallogr. Rep. **58** (1), 160 (2013).

32. H. Jeong and E. D. Williams, Surf. Sci. Rep. **34**, 171 (1999).

33. V. P. Vlasov, A. E. Muslimov, A. V. Butashin, and V. M. Kanevskii, Crystallogr. Rep. **61** (1), 58 (2016).

34. K. Maruyama, M. Yoshikawa, and H. Takigawa, J. Cryst. Growth **93**, 761 (1988).

35. K. K. Kim, J. H. Song, H. J. Jung, et al., J. Vac. Sci. Technol. A **18** (6), 2864 (2000).

36. J. Zuniga-Perez, R. Tena-Zaera, and V. Munoz-San-jose, J. Cryst. Growth **270**, 309 (2004).

37. Y. Wang, S. Wang, S. Zhou, et al., Appl. Surf. Sci. **253**, 1745 (2006).

38. S. Neretina, R. A. Hughes, J. F. Britten, et al., Appl. Phys. A **96**, 429 (2009).

39. T. Trautnitz, R. Sorgenfrei, and M. Fiederle, J. Cryst. Growth **312**, 624 (2010).

40. E. N. Maslen, V. A. Streltsov, N. R. Streltsova, et al., Acta Crystallogr. B **29**, 973 (1993).

41. H. Karzel, W. Potzel, M. Köfferlein, et al., Phys. Rev. B **53**, 11425 (1996).

42. M. Kh. Rabadanov, I. A. Verin, Yu. M. Ivanov, and V. I. Simonov, Crystallogr. Rep. **46** (4), 636 (2001).

43. V. I. Mikhailov, A. V. Butashin, V. M. Kanevskii, et al., Poverkhnost, No. **6**, 97 (2011).

44. A. V. Butashin, V. M. Kanevskii, A. E. Muslimov, et al., Crystallogr. Rep. **59** (3), 418 (2014).

45. A. E. Muslimov, A. V. Butashin, A. B. Kolymagin, et al., Crystallogr. Rep. **61** (1), 63 (2016).

46. M. Ying, X. Du, Z. Mei, et al., J. Phys. D **37**, 3058 (2004).

47. A. V. Butashin, V. M. Kanevskii, A. E. Muslimov, et al., Crystallogr. Rep. **60** (4), 565 (2015).

48. *Nanowires and Nanobelts, in: Materials, Properties and Devices,* Ed. by Z. L. Wang (Kluwer, USA, 2003).

49. F. Cuccureddu, S. Murphy, M. Porcu, and H. W. Zand-bergen, Nano Lett. **8** (10), 3248 (2008).

50. Y. Qin, S.-M. Lee, A. Pan, et al., Nano Lett. **8** (1), 114 (2008).

51. J. Hu, T. W. Odom, and C. M. Lieber, Acc. Chem. Res. **32**, 435 (1999).

52. S. Link and M. A. El-Sayed, J. Phys. Chem. B **103**, 8410 (1999).

53. G. F. Bakanov and G. V. Petrova, *Photolithography* (Izd-vo SPb GETU LETI, St. Petersburg, 2002) [in Russian].

54. A. E. Muslimov, A. V. Butashin, A. A. Konovko, et al., Crystallogr. Rep. **57** (3), 415 (2012).

55. A. E. Muslimov, A. V. Butashin, A. Yu. Kolymagin, et al., Kristallografiya **60** (6), 958 (2015).

56. Y. H. Kim, H. Ruh, Y. K. Noh, et al., J. Appl. Phys. **107**, 063501 (2010).

57. Y. P. Hsua, S. J. Changa, Y. K. Sua, et al., J. Cryst. Growth **261**, 466 (2004).

58. Y.-K. Ee, X.-H. Li, J. Biser, et al., J. Cryst. Growth **312**, 1311 (2010).

59. A. V. Butashin, V. M. Kanevskii, A. E. Muslimov, et al., Crystallogr. Rep. **59** (5), 732 (2014).

60. A. E. Muslimov, A. V. Butashin, R. G. Valeev, et al., *Proc. XXVI Russ. Conf. on Electron Microscopy (RKEM-2016), Moskva, Zelenograd, 2016.*

61. A. Erko, M. Idir, Th. Krist, and A. G. Michette, Springer Ser. Opt. Sci., No. 137 (2008).

62. B. S. Roshchin, V. E. Asadchikov, A. E. Blagov, et al., *Proc. Meeting "X-Ray Optics–2010," Chernogolovka, 20–23 Sept. 2010,* p. 122.

63. A. V. Vinogradov and I. V. Kozhevnikov, Tr. FIAN **196**, 31 (1989).

64. O. M. Suleimenov, Rev. Sci. Instrum. **75**, 3363 (2004).

65. S. Hosokawa and W.-C. Pilgrim, Nucl. Instrum. Methods Phys. Res., Sect. A **467−468**, 1057 (2001).

66. V. E. Asadchikov, A. V. Butashin, A. V. Buzmakov, et al., Cryst. Res. Technol. **51** (4), 290 (2016).

Translated by Yu. Sin'kov